Freie Universität Berlin

Title:

Mechanism of collective interstitial ordering in Fe–C alloys

Author(s):

Xie Zhang, Hongcai Wang, Tilmann Hickel, Jutta Rogal, Yujiao Li & Jörg Neugebauer

Document type: Preprint

Citation:

Mechanism of collective interstitial ordering in Fe-C alloys

Xie Zhang[1,3,*], Hongcai Wang[2,*], Tilmann Hickel[3], Jutta Rogal[4], Yujiao Li[5], and Jörg Neugebauer[3]

[1]Materials Department, University of California, Santa Barbara, California 93106-5050, USA

[2]Institut für Werkstoffe, Ruhr-Universität Bochum, Bochum, 44801, Germany

[3]Max-Planck-Institut für Eisenforschung GmbH, 40237 Düsseldorf, Germany

[4]Interdisciplinary Centre for Advanced Materials Simulation, Ruhr-Universität Bochum, 44780 Bochum, Germany

[5]ZGH, Ruhr-Universität Bochum, Bochum, 44801, Germany

[*] e-mail: xiezhang@ucsb.edu; e-mail: hongcai.wang@rub.de

Collective interstitial ordering is at the core of martensite formation in Fe-C-based alloys, laying the foundation for high-strength steels. Even though this ordering has been studied extensively for more than a century, some fundamental mechanisms remain elusive. Here, we evidence the unexpected effects of two correlated phenomena on the ordering mechanism: anharmonicity and segregation. The local anharmonicity in the strain fields induced by interstitials significantly reduces the critical concentration for interstitial ordering, up to a factor of three. Further, the competition between interstitial ordering and segregation results in an effective decrease of interstitial segregation to extended defects for high interstitial concentrations. The mechanism and corresponding impact on interstitial ordering identified here enrich the theory of phase transitions in materials and constitute a crucial step in the design of ultrahigh-performance alloys.

Alloying is one of most efficient ways to improve the structural and electronic properties of materials. The alloying atoms enter the host lattice as interstitials or substitutionals. Due to differences in the chemistry and atomic sizes, each interstitial or substitutional atom creates a local strain field, displacing its neighboring host atoms away from their original lattice positions. At high alloying concentrations, the interstitial or subsitutional atoms strongly interact with each other both chemically and elastically, leading to ordering/disordering phenomena and severe lattice distortions. This concept is often employed in designing, e.g., phase-change materials [1], battery electrode materials [2], and high-entropy alloys [3]. However, even at dilute alloying concentrations the interstitial or substitutional atoms can still interact via the host lattice, mediated by long-range strain induced interactions between the local distortion fields. An interplay between short-range chemical interaction and long-range strain induced interaction may lead to an ordering of interstitial or substitutional atoms, significantly impacting the performance of materials [4–7]. For instance, the presence of ordered oxygen complexes may simultaneously enhance the strength and ductility of alloys by changing their microscopic deformation mechanism [7]. Interstitials interact not only with each other, but, in real materials, also with extended defects, leading to interstitial segregation and a competition between interstitial segregation and ordering. Understanding the mechanism of the collective interstitial ordering is thus key in designing ultrahigh-performance alloys.
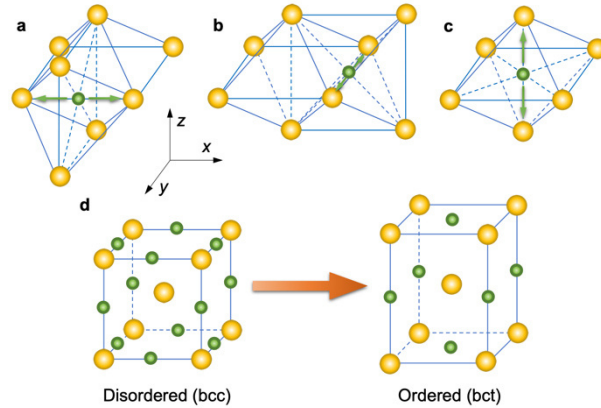
Fig. 1 | Disorder-order transition in Fe-C alloys. a-c, C occupation on three octahedral sublattices and its induced tetragonal deformation (green arrows). Large orange spheres denote Fe atoms and small green spheres refer to C atoms. **d**, Schematic illustration of the disorder-order transition. Green spheres show the possible sites for C to randomly occupy in a unit cell, but they are not all occupied.

A prototype of broad interest for interstitial ordering is the Fe-C system [8, 9], which is the central ingredient for advanced steels [10–12]. C atoms occupy octahedral interstitial sites in body-centered cubic (bcc) Fe, and there exist three octahedral sublattices (Fig. 1a-c) associated with a local tetragonal distortion along the three principal axes [13]. When C atoms randomly occupy the three sublattices (Fig. 1d), a disordered bcc phase is formed. Once the C concentration reaches a critical value, all C atoms occupy only one sublattice in bcc Fe (Fig. 1d), and the bcc phase transforms to an ordered body-centered tetragonal (bct) phase [14]. Although steels have been extensively researched for more than a century, and the above-mentioned phase transition is basic textbook knowledge in materials science, the ordering mechanism of C atoms in Fe is still actively debated [15–19].

Here, we identify two components that significantly affect the collective interstitial ordering. First, the strain fields induced by C interstitials in bcc Fe reveal pronounced anharmonicity, which reduces the critical C concentration of the disorder-order transition by 2–3 times. Second, C segregation to extended defects is favorable at low C concentrations, but it is strongly suppressed due to a lowering of the C chemical potential in the ordered martensite at high C concentrations. Both the surprising magnitude of the anharmonic contributions and the abrupt change in segregation behavior are decisive for the transformation mechanism and constitute important fundamental knowledge about phase transitions in general.

To capture all aspects of the complex mechanism underlying the collective interstitial ordering, a set of computational approaches needs to be developed. We will start by establishing a reliable methodology for interstitial interactions and ordering, and subsequently determine the impact of anharmonicity on the interstitial ordering. Further, we will formulate a self-consistent defect-chemistry (SC) approach that allows us to investigate the competition between interstitial ordering and segregation.

An efficient approach to computing the interactions between point defects is based on the microscopic elasticity theory (MET) developed by Khachaturyan [20]. The long-range strain induced (si) interaction between two interstitials separated by $\mathbf{R}$ in a bcc lattice is computed by

$$V_{mn}^{\text{si}}(\mathbf{R}) = \frac{1}{N} \sum_{\mathbf{q}} V_{mn}^{\text{si}}(\mathbf{q}) e^{i\mathbf{q}\mathbf{R}} \qquad (1)$$

$$V_{mn}^{\text{si}}(\mathbf{q}) = -\mathbf{F}_m(\mathbf{q})\mathbf{G}(\mathbf{q})\mathbf{F}_n^*(\mathbf{q}) + Q_{mm}\delta_{mn} \qquad (2)$$

where Q_{mm} is the self-interaction correction:

$$Q_{mm} = \frac{1}{N} \sum_{\mathbf{q}} \mathbf{F}_m(\mathbf{q})\mathbf{G}(\mathbf{q})\mathbf{F}_m^*(\mathbf{q}) \qquad (3)$$

$\mathbf{G}(\mathbf{q})$ are the Fourier components of the lattice Green's function at $\mathbf{q}$ in reciprocal space. $\mathbf{F}(\mathbf{q})$ are the Fourier components of the equivalent forces on the host Fe lattice inducing the lattice distortion generated by an interstitial, commonly referred to as Kanzaki forces [21, 22]. m and n are the sublattice indices of two interstitial atoms. N is the total number of $\mathbf{q}$ points. δ_{mn} is the Kronecker delta.

To calculate the strain induced interaction the major tasks comprise the computation of the lattice Green's function and Kanzaki forces. Conventionally, the lattice Green's function and Kanzaki forces are obtained using analytical formulas for a particular defect and host lattice (see Supplementary Note 1). This is computationally very efficient, but not sufficiently accurate and lacks generalizability and transferability. Hence, we generalize MET by computing the lattice Green's function and Kanzaki forces from atomistic calculations. To benchmark the accuracy of our approach, we also compute the strain induced interaction directly from atomistic calculations using a carefully tested embedded atom method (EAM) potential [23].
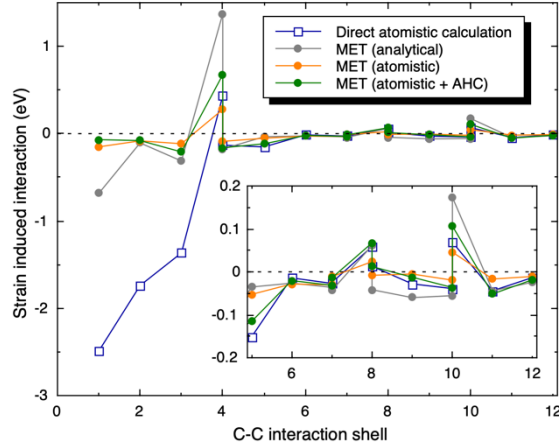
Fig. 2 | Strain induced interaction. Strain induced interaction between two C interstitials in bcc Fe from different approaches. The inset provides an enlarged view for the interactions at the 5th–12th shells. "AHC" stands for anharmonic contribution.

Figure 2 shows the strain induced interaction between two C interstitials in bcc Fe calculated with these different approaches. Clearly, MET completely fails for the first three interaction shells. This is understandable since when two

interstitials are too close to each other, linear elasticity theory does not apply. However, even if we focus on larger separation distances, MET is still insufficiently accurate, especially when we use an analytical parametrization. By using Kanzaki forces and a lattice Green's function obtained from atomistic calculations, the accuracy of MET is improved, but still unsatisfactory. To narrow down the origin of the discrepancy, we inspect the lattice Green's function and Kanzaki forces individually. We find that the discrepancy in the long-range strain induced interaction does not stem from the lattice Green's function (see Supplementary Note 2).
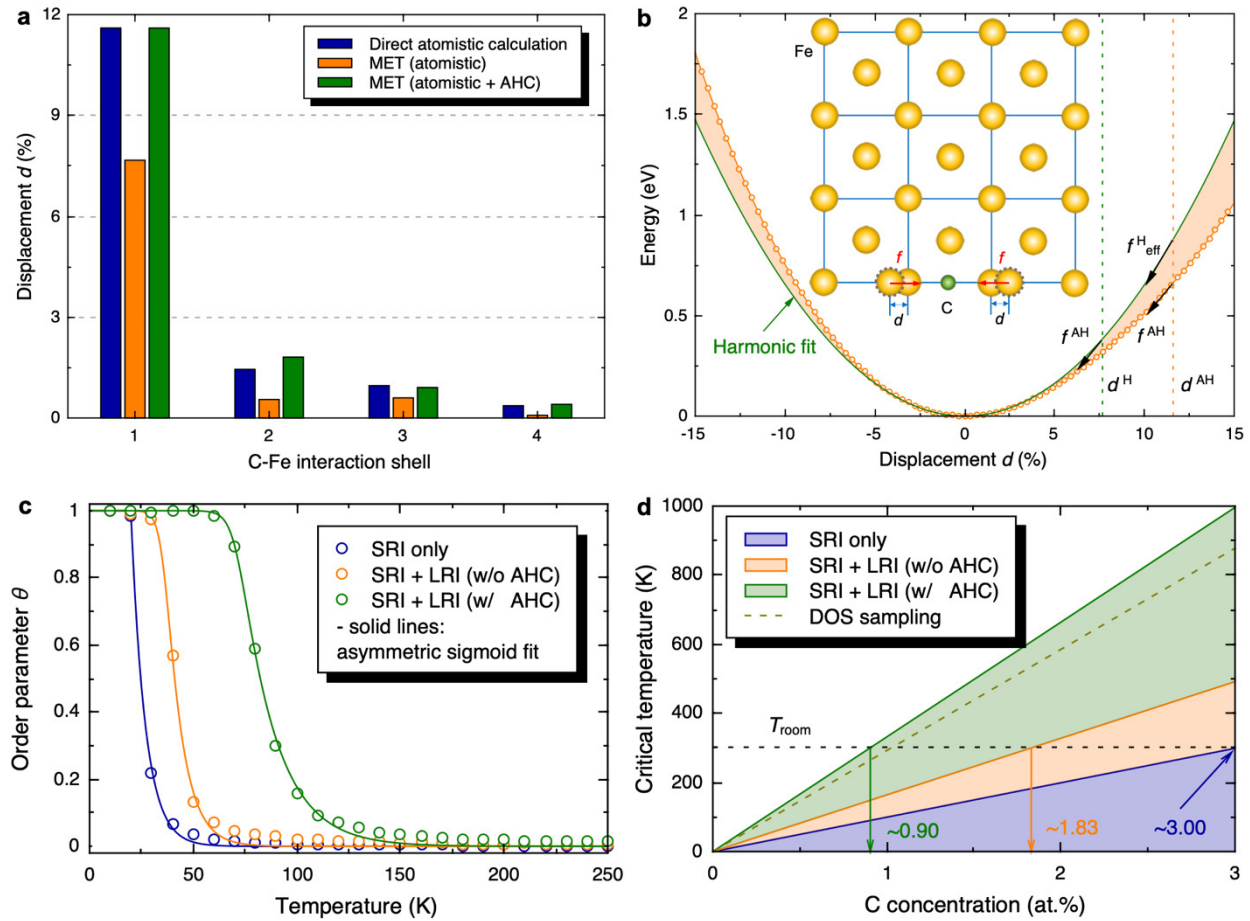
Fig. 3 | Impact of local anharmonicity on the disorder-order transition. a, Displacements of Fe atoms at different interaction shells around a C interstitial in bcc Fe. **b**, Anharmonic potential energy surface of the Fe lattice as a function of the displacement of the first-nearest-neighbor Fe atoms induced by a C interstitial. The inset schematically shows the local displacements (d) and forces (f) of the first-nearest-neighbor Fe atoms induced by the C interstitial. The sign of d indicates whether the first-nearest-neighbor Fe atoms displace away from (positive) or toward (negative) the C atom. f^{AH} is the anharmonic force at the displacement d^{AH}. d^{H} is the resulting harmonic displacement associated with f^{AH}. f_{eff}^{H} is the effective harmonic force in order to achieve the anharmonic displacement d^{AH}. **c**, Simulated order parameter as a function of temperature for three scenarios for a representative C concentration of 0.3 at.%. "SRI" and "LRI" stand for short-range and long-range interaction, respectively. "AHC" refers to anharmonic contribution. **d**,

Calculated critical temperature as a function of C concentration in comparison with the result obtained from the density of states (DOS) sampling approach.

Figure 3a presents the displacements (in percentage of the lattice constant) of the neighboring Fe atoms induced by a C interstitial computed with different methods. The displacement of the host Fe atoms at the first interaction shell obtained from atomistic calculations is ~11.6%, similar to the value from DFT, ~12.6%, which confirms that the large displacement is not an artifact of the EAM potential. The displacement is so large that the linear elasticity theory (on which MET is based) may not apply anymore. Even if we use input from atomistic calculations, the displacement of the first-nearest-neighbor Fe atoms computed from MET [i.e., $\mathbf{d}(\mathbf{R}) = 1/N \sum_{\mathbf{q}} \mathbf{G}(\mathbf{q}) \mathbf{F}^*(\mathbf{q}) e^{i\mathbf{qR}}$] is still much smaller than the one from atomistic relaxations.

More intuitively, we can directly map the potential energy surface of the Fe lattice as a function of the displacement of the first-nearest-neighbor Fe atoms. As shown by the comparison between the orange line and its harmonic fit (within ±1% displacements) in Fig. 3b, the potential energy surface is highly asymmetric at large displacements. As a result, when using the Kanzaki forces (f^{AH}) obtained at large displacements (d^{AH}) on the anharmonic potential energy surface to compute the harmonic displacement with MET, the actual displacement is only d^{H} (Fig. 3b). Apparently, the displacement is underestimated, which as we will show is the origin of the discrepancy in the long-range strain induced interaction. To account for the anharmonic contribution and recover the correct strain field induced by a C interstitial, we need to use an effective Kanzaki force ($f^{\mathrm{H}}_{\mathrm{eff}}$) in the harmonic MET. By taking into account the anharmonic contribution in the first-neighbor shell, the subsequent displacements of Fe atoms at different interaction shells are much better captured. Moreover, the accuracy of the strain induced interaction is significantly improved, showing excellent agreement with our benchmarking result (Fig. 2). Qualitatively, we have also observed such strong lattice distortions in high-resolution transmission electron microscopy images (see Supplementary Note 3 and Fig. 2).

Having established the above approach for the long-range strain induced interaction between two C interstitials, we set up an Ising-type Hamiltonian and efficiently simulate the disorder-order transition with Monte Carlo sampling. This methodology overcomes the limitation of standard Ising-type Hamiltonians with pair interactions truncated at certain distances.

Figure 3c shows the order parameter (θ) as a function of temperature for three scenarios at a representative C concentration, 0.3 at.%. In the first scenario, we only take into account the short-range interactions ($\leq 7^{\mathrm{th}}$ shell, blue curve) and ignore the long-range strain induced interactions. As a comparison, for the other two scenarios we further include the long-range strain induced interactions computed from MET without (orange) and with (green) the anharmonic contribution for the first-nearest neighbors. It is evident that even though C tends to be ordered for the first scenario, the critical temperature is very low. We plot the critical temperatures as a function of C concentration in Fig. 3d. At room temperature, the critical C concentration for the disorder-order transition including only short-

range interactions is ~3 at.%, which is very high, indicating that the formation of ordered Fe-C martensite would be unlikely at low C concentrations and mainly driven by one particular attractive C-C interaction at the 7th shell (see Supplementary Fig. 3). When we include the long-range strain induced interaction without the anharmonic contribution, the ordered Fe-C martensite is stabilized and the critical C concentration at room temperature is reduced to ~1.8 at.%. This makes the formation of ordered martensite easier, but the critical concentration is still much higher than dilute C conditions (<1 at.%). However, once we include the anharmonic contribution, the critical C concentration at room temperature is significantly reduced to 0.9 at.%. In principle, even for the first two scenarios the impact of the local anharmonicity is partly included, since the displacement of the first-nearest-neighbor Fe atom in this case falls already within the anharmonic region (Fig. 3a). Hence, overall the local anharmonicity in the C-induced strain fields reduces the critical C concentration by a factor of 2–3, which is an unexpectedly large effect.

To cross-validate the accuracy of our Monte Carlo simulations, we calculate the critical temperature of the disorder-order transition with a density of states (DOS) sampling approach using the same EAM potential (see Supplementary Note 4). The comparison in Fig. 3d shows that the two independent approaches yield very similar results. Since within the DOS sampling approach anharmonicity is implicitly included, the agreement indicates that MET with anharmonic contribution correctly captures the C interactions.
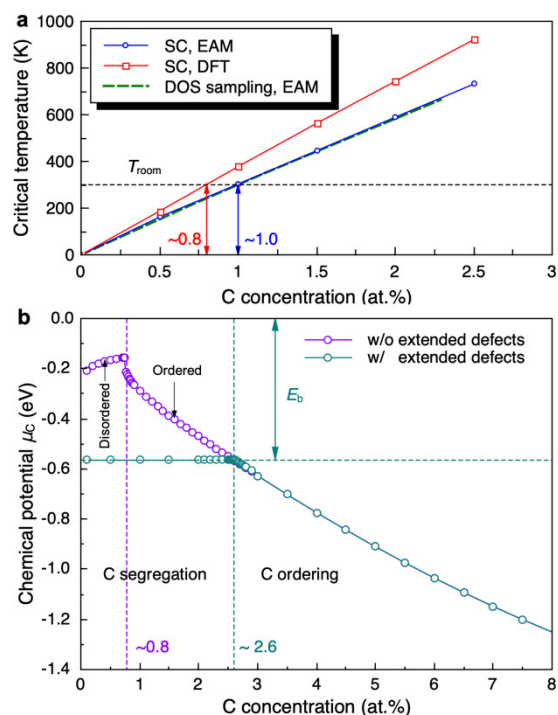

Fig. 4 | Competition between C ordering and segregation. a, Calculated critical temperature as a function of C concentration using the self-consistent defect-chemistry ("SC") approach with EAM or DFT input compared to the result obtained from the DOS sampling approach. **b**, Chemical potential of C (μ_C) at room temperature as a function

of C concentration computed from the SC approach with DFT input. The μ_C in bcc Fe at $T = 0$ K is used as zero energy reference. E_b is the binding energy between a C interstitial and an extended defect.

The critical C concentration derived above corresponds to the net C concentration in the matrix, which is different from the nominal C concentration, since C can also segregate to extended defects such as dislocations and grain boundaries. As a second aspect to establish a comprehensive understanding of the mechanism, we consider the competition between C solution in the matrix and its segregation to extended defects. To achieve this, we have developed a SC approach (see Supplementary Note 5) for the chemical potential of C in the disordered/ordered martensite, which can be directly compared with the chemical potential of C at extended defects. We benchmark the accuracy of the SC approach against the DOS sampling results. Using the same EAM potential the two approaches produce very consistent results (Fig. 4a), validating the reliability of the SC approach. With the SC approach we can further improve the accuracy of our results by using DFT input, yielding a critical C concentration of 0.8 at.% at room temperature, which is slightly lower than the one (1.0 at.%) obtained using EAM input.

Figure 4b shows the calculated chemical potential of C (μ_C) at room temperature as a function of C concentration. First, μ_C in Fe-C martensite gradually increases with increasing C concentration, until at 0.8 at.% μ_C starts to rapidly decrease, corresponding to the disorder-order transition. At extended defects μ_C is constant for low C concentrations when the C-C interaction at the defect is small and can be determined by the binding energy (E_b) between C and an extended defect, i.e., $\mu_C = -E_b$. By taking an averaged value for E_b from existing literature [24–30], we find that the μ_C at extended defects is much lower than that in the disordered martensite and is competitive against the ordered martensite at C concentrations below ~2.6 at.%. This, in principle, indicates that below ~2.6 at.% no Fe-C martensite can form. However, there is a limit for the amount of C atoms that extended defects can accommodate. It is challenging to determine the exact value from theory, since it depends on the density of extended defects. According to experiments [31,32], the limit is around 0.8 at.%. We note that this value of 0.8 at.% is only by coincidence equal to the critical C concentration of the disorder-order transition at room temperature, but the two values have clearly different meanings. Hence, above ~0.8 at.% the excess C triggers the formation of disordered martensite, which transforms to ordered martensite at ~1.6 at.% (0.8 at.% trapped at defects + 0.8 at.% triggering the disorder-order transition). Furthermore, after reaching 2.6 at.%, C segregation to extended defects is suppressed, since it is energetically more favorable for C to form ordered martensite.
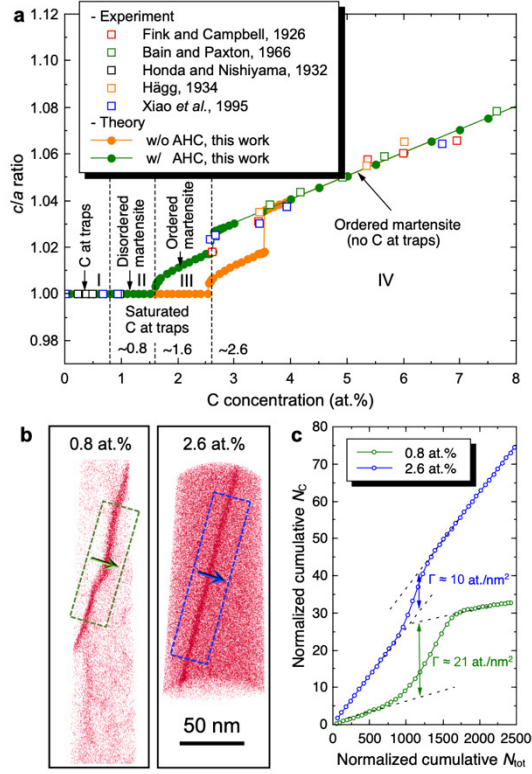
Fig. 5 | Comparison between theory and experiment. a, Comparison of experimental and theoretically computed *c/a* ratio of Fe-C alloys as a function of C concentration at room temperature. The experimental data are collected from refs. [33-37]. **b**, APT analysis of the C distribution in two representative alloy samples with 0.8 and 2.6 at.% C. The regions highlighted by the green ($30 \times 26 \times 94$ nm^3) and blue ($30 \times 37 \times 131$ nm^3) rectangles along the grain boundaries are selected for a quantitative analysis of C excess. **c**, Gibbsian interfacial excess of C for the two alloy samples. N_C and N_{tot} are the cumulative number of C and of all atoms, respectively, normalized by the selected grain boundary areas.

To verify the mechanism proposed above, we compare our theoretically predicted *c/a* ratio of Fe-C alloys as a function of C concentration at room temperature with experiment [33–37] in Fig. 5a. We divide this plot into four distinct regimes. In regime I (<~0.8 at.% C), C is trapped at extended defects, and the bulk region is primarily comprised of pure Fe, which thus has a *c/a* ratio of 1. In regime II (0.8−1.6 at.%), disordered martensite and C saturated traps coexist, leading to a *c/a* ratio of 1 as well. In regime III (1.6−2.6 at.%), ordered martensite becomes energetically more favorable than the disordered one, coexisting with C saturated traps. The *c/a* ratio is already larger than 1, but since it is still relatively small, it is experimentally difficult to determine the exact *c/a* ratio by fitting slightly split X-ray diffraction peaks [37]. In regime IV (>~2.6 at.%), fully ordered martensite is formed with negligible C segregation to extended defects, which is supported by the fact that the experimental *c/a* ratios agree well with those of the fully ordered martensite across a large range of C concentrations. We also show that if the anharmonic contribution is neglected [38], the critical C concentrations for the transitions of regime II ↔ III and III ↔ IV are shifted upward by ~0.93 at.%, strongly deviating from the experimental data.

Our proposed mechanism of a competition between C segregation and ordering is also compatible with atom probe tomography (APT) experiments. We analyze the distribution of C atoms across the geometrically necessary dislocations (GNDs) in grain boundaries for samples with two representative C concentrations (0.8 and 2.6 at.%). For a low C concentration of 0.8 at.%, C atoms strongly segregate to the GNDs, while they are more homogeneously distributed in the sample with 2.6 at.% C (Fig. 5b). To quantitatively compare the excess of segregation between samples with different C concentrations, we analyze the Gibbsian interfacial excess of C atoms (Γ), i.e., the number of excess C atoms per grain boundary area [39].

Figure 5c shows the cumulative number of C atoms vs. that of all atoms along the grain boundary normal (see the arrows in Fig. 5b). For samples without segregation, i.e., with a C concentration in the defect that is identical to that of the bulk, a straight line with a slope equal to the C concentration is expected. The steps observed in both curves imply C segregation and allow us to quantify Γ in each sample. Based on our theoretical calculations (Fig. 5a), the low-C sample is located between regime I and II; C atoms are mostly segregated to extended defects, which implies a large Γ. In contrast, the high-C sample sits at the border between regime III and IV; the chemical potentials of C in extended-defect-free bulk and at extended defects are comparable (Fig. 4b), which indicates only a slight accumulation of C at the GNDs inside the grain boundary and thus a very small Γ. Indeed, by increasing the C concentration from 0.8 to 2.6 at.%, Γ decreases from 21 to 10 at./nm^2. We note that the grain boundary roughness in the low-C sample has only a minor impact on Γ. To account for the interface roughness, we average over several flat regions, yielding a Γ value of 20±2 at./nm^2 (see Supplementary Fig. 10), which encompasses the value estimated over the entire grain boundary region (the green rectangle in Fig. 5b).

The above analysis has two important implications: i) there is significant C segregation to extended defects at low C concentrations, which cannot be ignored; and ii) C segregation to extended defects at high C concentrations is suppressed due to the formation of energetically favorable ordered Fe-C martensite. The exact critical C concentrations also depend on the microstructure of the material sample and the binding energy between C and a specific extended defect. Hence, the two critical concentrations derived in Fig. 5a are not universal across different samples and extended defects. Nevertheless, if an estimate of the exact binding energy between C and the extended defect and the maximum C concentration that can be accommodated by the extended defect is accessible, the critical concentrations can be rigorously derived using the SC approach presented in Fig. 4.

In conclusion, we have elucidated the role of anharmonicity and segregation in the mechanism of interstitial ordering in Fe-C alloys. The local anharmonicity in the strain field induced by interstitials significantly stabilizes the collective interstitial ordering. Furthermore, interstitial segregation to extended defects predominates over interstitial ordering at low interstitial concentrations, but is strongly suppressed at high interstitial concentrations. This somewhat counter-intuitive behavior can be understood from the chemical potential of the interstitials in ordered martensite, which rapidly decreases with increasing interstitial concentration. Our results clearly show that theoretical concepts to

compute accurate critical temperatures or concentrations of disorder-order phase transitions in interstitial alloys require the inclusion of anharmonic effects, which is presently not standard. Disorder-order phase transitions are relevant not only in interstitial alloys but for a wide range of materials. Examples are substitutional ordering in high-entropy alloys [40], cation ordering in perovskites [41], and vacancy ordering in various oxides [5]. Since in all these systems large relaxations occur, anharmonic effects will be important and affect phase transition temperatures. Thus, only when these effects are included, predictive materials design becomes possible.

References

1. Wuttig, M., Lüsebrink, D., Wamwangi, D., Welnic, W., Gillßen, M., & Dronskowski, R. The role of vacancies and local distortions in the design of new phase-change materials. *Nat. Mater*. **6**, 122–128 (2007).

2. Guignard, M., Didier, C., Darriet, J., Bordet, P., Elkam, E., & Delmas, C. P2-Na_xVO_2 system as electrodes for batteries and electron-correlated materials. *Nat. Mater*. **12**, 74–80 (2013).

3. Sohn, S. S., Kwiatkowski da Silva, A., Ikeda, Y., Körmann, F., Lu, W., Choi, W. S., Gault, B., Ponge, D., Neugebauer, J., & Raabe, D. Ultrastrong medium-entropy single-phase alloys designed via severe lattice distortion. *Adv. Mater*. **31**, 1807142 (2019).

4. Siegrist, T., Jost, P., Volker, H., Woda, M., Merkelbach, P., Schlockermann, C., & Wuttig, M. Disorder-induced localization in crystalline phase-change materials. *Nat. Mater*. **10**, 202–208 (2011).

5. Li, X., Ma, X., Su, D., Liu, L., Chisnell, R., Ong, S. P., Chen, H., Toumar, A., Idrobo, J.-C., Lei, Y., Bai, J., Wang, F., Lynn, J. W., Lee, Y. S., & Ceder, G. Direct visualization of the Jahn-Teller effect coupled to Na ordering in $Na_{5/8}MnO_2$. *Nat. Mater*. **13**, 586–592 (2014).

6. Ni, Y. & Khachaturyan, A. G. From chessboard tweed to chessboard nanowire structure during pseudospinodal decomposition. *Nat. Mater*. **8**, 410–414 (2009).

7. Lei, Z., Liu, X., Wu, Y., Wang, H., Jiang, S., Wang, S., Hui, X., Wu, Y., Gault, B., Kontis, P., Raabe, D., Gu, L., Zhang, Q., Chen, H., Wang, H., Liu, J., An, K., Zeng, Q., Nieh, T.-G., & Lu, Z. Enhanced strength and ductility in a high-entropy alloy via ordered oxygen complexes. *Nature* **563**, 546–550 (2018).

8. Seljakow, N. The nature of martensite. *Nature* **123**, 204–205 (1929).

9. Jack, K. H. Iron-nitrogen, iron-carbon and iron-carbon-nitrogen interstitial alloys: their occurrence in tempered martensite. *Nature* 158, 60 (1946).

10. Li, Y., Raabe, D., Herbig, M., Choi, P.-P., Goto, S., Kostka, A., Yarita, H., Borchers, C., & Kirchheim, R. Segregation stabilizes nanocrystalline bulk steel with near theoretical strength. *Phys. Rev. Lett.* **113**, 106104 (2014).

11. Zhang, X., Hickel, T., Rogal, J., Fähler, S., Drautz, R., & Neugebauer, J. Structural transformations among austenite, ferrite and cementite in Fe-C alloys: A unified theory based on ab initio simulations. *Acta Mater*. **99**, 281–289 (2015).

12. Wang, H., Zhang, X., Yan, D., Somsen, C., & Eggeler, G. Interface dominated cooperative nanoprecipitation in interstitial alloys. *Nat. Commun*. **9**, 4107 (2018).

13. Zhang, X., Hickel, T., Rogal, J., & Neugebauer, J. Interplay between interstitial displacement and displacive lattice transformations. *Phys. Rev. B* **94**, 104109 (2016).

14. Honda, K. & Sekito, S. Two kinds of martensite. *Nature* **121**, 744–744 (1928).

15. Udyansky, A., von Pezold, J., Bugaev, V. N., Friák, M., & Neugebauer, J. Interplay between long-range elastic and short-range chemical interactions in Fe-C martensite formation. *Phys. Rev. B* **79**, 224112 (2009).

16. Udyansky, A., von Pezold, J., Dick, A., & Neugebauer, J. Orientational ordering of interstitial atoms and martensite formation in dilute Fe-based solid solutions. *Phys. Rev. B* **83**, 184112 (2011).

17. Naraghi, R., Selleby, M., & Ågren, J. Thermodynamics of stable and metastable structures in Fe-C system. *Calphad* **46**, 148–158 (2014).

18. Ruban, A. V. Self-trapping of carbon atoms in α-Fe during the martensitic transformation: A qualitative picture from ab initio calculations. *Phys. Rev. B* **90**, 144106 (2014).

19. Djaziri, S., Li, Y., Nematollahi, G. A., Grabowski, B., Goto, S., Kirchlechner, C., Kostka, A., Doyle, S., Neugebauer, J., Raabe, D., & Dehm, G. Deformation-induced martensite: A new paradigm for exceptional steels. *Adv. Mater*. **28**, 7753–7757 (2016).

20. Khachaturian, A. Theory of structural transformations in solids (Wiley, New York, 1983).

21. Kanzaki, H. Point defects in face-centred cubic lattice-II X-ray scattering effects. *J. Phys. Chem. Solids* **2**, 107–114 (1957).

22. Kanzaki, H. Point defects in face-centred cubic lattice-I distortion around defects. *J. Phys. Chem. Solids* **2**, 24–36 (1957).

23. Lau, T. T., Först, C. J., Lin, X., Gale, J. D., Yip, S., & Vliet, K. J. V. Many-body potential for point defect clusters in Fe-C alloys. *Phys. Rev. Lett.* **98**, 215501 (2007).

24. Cochardt, A., Schoek, G., & Wiedersich, H. Interaction between dislocations and interstitial atoms in body-centered cubic metals. *Acta Metall*. **3**, 533–537 (1955).

25. Kamber, K., Keefer, D., & Wert, C. Interactions of interstitials with dislocations in iron. *Acta Metall*. **9**, 403–414 (1961).

26. Douthwaite, R. & Evans, J. Interaction between a tetragonal distortion and a ⟨111⟩ screw dislocation in an anisotropic cubic crystal. *Scr. Mater.* **7**, 1019–1026 (1973).

27. de Hosson, J. An atomic model for the interaction between a 12 ⟨111⟩ {110} edge dislocation and carbon in α-Fe. *Solid State Commun.* **17**, 747–750 (1975).

28. Tapasa, K., Osetsky, Y., & Bacon, D. Computer simulation of interaction of an edge dislocation with a carbon interstitial in α-iron and effects on glide. *Acta Mater*. **55**, 93–104 (2007).

29. Clouet, E., Garruchet, S., Nguyen, H., Perez, M., & Becquart, C. S. Dislocation interaction with C in α-Fe: A comparison between atomic simulations and elasticity theory. *Acta Mater*. **56**, 3450–3460 (2008).

30. Lejček, P. Grain boundary segregation in metals (Springer Berlin Heidelberg, Berlin, Heidelberg, 2010).

31. Speich, G. R. Tempering of low-carbon martensite. *Trans. TMS-AIME* **245**, 2553–2564 (1969).

32. Wilde, J., Cerezo, A., & Smith, G. D. W. Three-dimensional atomic-scale mapping of a cottrell atomosphere around a dislocation in iron. *Scr. Mater*. **43**, 39– 48 (2000).

33. Fink, W. L. & Campbell, E. D. Influence of heat treatment and carbon contents on the structure of pure iron-carbon alloys. *Trans. Am. Soc. Steel Treat*. **9**, 717–748 (1926).

34. Bain, E. C. & Paxton, H. W. Alloying Elements in Steel (ASM, Ohio, 1966).

35. Honda, E. & Nishiyama, Z. On the nature of the tetragonal and cubic martensites. *Sci. Rep. Toh. Imper. Univ.* **21**, 299–331 (1932).

36. Hägg, G. X-ray investigations on the structure and decomposition of martensite. *J. Iron Steel Inst.* **130**, 439– 451 (1934).

37. Xiao, L., Fan, Z., Jinxiu, Z., Mingxing, Z., Mokuang, K., & Zhenqi, G. Lattice-parameter variation with carbon content of martensite. I. X-ray-diffraction experimental study. *Phys. Rev. B* **52**, 9970–9978 (1995).

38. We note that with the SC approach anharmonicity is inherently included. The difference in the *c/a* ratio caused by anharmonicity as presented in Fig. 5a is derived from the results in Fig. 3d.

39. Krakauer, B. W. & Seidman, D. N. Absolute atomic-scale measurements of the Gibbsian interfacial excess of solute at internal interfaces. *Phys. Rev. B* **48**, 6724–6727 (1993).

40. Santodonato, L. J., Liaw, P. K., Unocic, R. R., Bei, H., & Morris, J. R. Predictive multiphase evolution in Al-containing high-entropy alloys. *Nat. Commun.* **9**, 4520 (2018).

41. King, G. & Woodward, P. M. Cation ordering in perovskites. *J. Mater. Chem.* **20**, 5785 (2010).

Methods

Direct computation of C-C interactions. To directly compute the C-C interactions, two C interstitials are placed at two octahedral sites (with sublattice indices m and n) separated by $\mathbf{R}$ in a 10×10×10 supercell of bcc Fe. The chemical interaction between the two C atoms is then computed by

$$V_{mn}^{\text{ch}}(\mathbf{R}) = E_{mn}^{\text{Fe+2C}}(\mathbf{R}) - E^{\text{Fe}} - 2(E^{\text{Fe+C}} - E^{\text{Fe}}) \quad (4)$$

where $E_{mn}^{\text{Fe+2C}}(\mathbf{R})$ and $E_{mn}^{\text{Fe+C}}$ are the energies of the systems containing two C interstitials separated by $\mathbf{R}$ and a single C atom in the Fe lattice, respectively. E^{Fe} is the energy of the Fe lattice. The three energies are computed with the same EAM potential [23] at the optimized lattice constant of bcc Fe (2.867 Å) and fixed atomic positions. All of the calculations with the EAM potential are performed using the LAMMPS package [42].

Similarly, we can also compute the total interactions [$V^{\text{tot}}(\mathbf{R})$] between two C interstitials using equation (4) but fully relax the atomic positions. Then the strain induced interactions [$V^{\text{si}}(\mathbf{R})$] between two C interstitials can be evaluated by

$$V_{mn}^{\text{si}}(\mathbf{R}) = V_{mn}^{\text{tot}}(\mathbf{R}) - V_{mn}^{\text{ch}}(\mathbf{R}) \quad (5)$$

MET calculations. The Kanzaki forces are computed by placing a C atom at an octahedral site of the three sublattices in a 10×10×10 supercell of bcc Fe, relaxing the atomic positions and evaluating the forces on the host Fe atoms after removing the C interstitial from the relaxed lattice. Then a Fourier transform is performed to compute the Fourier components of the Kanzaki forces on a 20×20×20 $\mathbf{q}$-point grid in reciprocal space, i.e.,

$$\mathbf{F}_m(\mathbf{q}) = \sum_j \mathbf{F}_{m,j}(\mathbf{R}'_j) e^{-i\mathbf{q}\mathbf{R}'_j} \quad (6)$$

where $\mathbf{F}_{m,j}(\mathbf{R}'_j)$ are the real-space Kanzaki forces on lattice site j of sublattice m. $\mathbf{R}'_j$ is the atomic coordinates of lattice site j relative to the location of the C interstitial and symmetrized by taking into account the periodic boundary condition.

The lattice Green's function is computed by inverting the dynamical matrix in reciprocal space on the same $20 \times 20 \times 20$ **q**-point grid. The dynamical matrix is computed by using a finite displacement method in real space with a $10 \times 10 \times 10$ supercell of bcc Fe and a 0.02 Bohr (0.0106 Å) displacement. A Fourier transform is performed to compute the reciprocal-space dynamical matrix and a Fourier interpolation is employed to obtain the dynamical matrix on the dense **q**-point grid as implemented in the S/PHI/nX package [43].

DFT calculations. Spin-polarized DFT calculations are performed using the Vienna *Ab-initio* Simulation Package (VASP) [44] to fully relax (shape, volume, and atomic positions) atomic structures using $4 \times 4 \times 4$ supercells of bcc Fe containing one C atom at an octahedral interstitial site or one Cr atom at a substitutional site. Projector augmented-wave (PAW) [45] pseudopotentials within the Perdew, Burke, and Ernzerhof (PBE) [46] parametrization are used. A plane-wave energy cutoff of 400 eV and a $5 \times 5 \times 5$ Monkhorst-Pack [47] **k**-point grid are employed to ensure convergences of total energy and forces. For structural relaxations, forces are minimized to below 0.01 eV/Å. Our DFT calculations indicate that the displacement of nearest-neighbor Fe atoms induced by a Cr substitutional atom is less than 1%, which is significantly smaller than the one induced by a C interstitial.

Sample preparation. The specimens for APT are fabricated using a dual beam focused-ion-beam (FIB) instrument (FEI Helios G4). The bulk sample is slightly etched using 5% Nital with a few drops of concentrated HCl acid to outline the grain boundaries. FIB milling is applied for site-specific preparation of APT samples containing (prior austenite) grain boundaries (see Supplementary Fig. 9). One grain boundary (shown in Fig. 5c) is cut in-situ and then milled to a needle-like tip with a size below 50 nm.

APT characterization. APT analysis is performed using a local electrode atom probe (LEAP 5000 XR, Cameca Instruments) in voltage mode at 75 K, using a pulse fraction of 20%, a pulse repetition rate of 200 kHz and detection rates of 0.005−0.01 atoms per pulse. The APT data is reconstructed and analyzed using the commercial IVAS 3.8.2 software.

Monte Carlo simulations. Metropolis Monte Carlo simulations are performed using the following Ising-type Hamiltonian.

$$H = E_{\text{Fe}}^{\text{tot}} + \frac{1}{2}\sum_{ij}^{i<j} V_{ij}^{\text{tot}}(\mathbf{R}_{ij}) \qquad (7)$$

where $E_{\text{Fe}}^{\text{tot}}$ is the total energy of the undistorted Fe lattice. $V_{ij}^{\text{tot}}(\mathbf{R}_{ij})$ is the total interaction energy between two C interstitials (indexed by i and j) separated by $\mathbf{R}_{ij}$. For the current Hamiltonian, we ignore the vibrational entropy difference between the ordered and disordered phases, since it is small compared to the configurational entropy difference and also beyond the current capability of sampling. Our tests for two representative ordered and disordered

configurations show a difference of ~2.5 meV/C atom at room temperature in the vibrational free energy, which is only around 3% of the total energy difference at $T = 0$ K between the ordered and disordered configurations (see Supplementary Fig. 7). When the distance between two C interstitials is shorter than a cut-off distance r_c, we use total interactions computed from the EAM potential, otherwise from the MET by inverse Fourier transforms, i.e.,

$$V^{tot}(\mathbf{R}) = \begin{cases} V^{tot}_{EAM}(\mathbf{R}), & |\mathbf{R}| \leq r_c \\ V^{ch}_{EAM}(\mathbf{R}) + \frac{1}{N}\sum_{\mathbf{q}} V^{si}_{mn}(\mathbf{q})e^{i\mathbf{qR}}, & |\mathbf{R}| > r_c \end{cases} \quad (8)$$

As the short-range chemical interaction vanishes after reaching the 7th interaction shell, we set r_c to the 7th interaction shell (see Supplementary Fig. 3).

We use a 10×10×10 supercell of bcc Fe including different number of C atoms. At each C concentration and each temperature, we sample 10^6 configurations in order to achieve a well-converged ensemble average of the order parameter. For each configuration sampled, the order parameter θ is defined as a combination of three sublattice order parameters [48], namely,

$$\theta = \frac{\sqrt{6}}{3}\sqrt{\theta_1^2 + \theta_2^2 + \theta_3^2} \quad (9)$$

where θ_1, θ_2 and θ_3 are three sublattice order parameters as given by

$$\theta_1 = x_1 - \frac{x_2+x_3}{2}, \theta_2 = x_2 - \frac{x_3+x_1}{2}, \theta_3 = x_3 - \frac{x_1+x_2}{2} \quad (10)$$

x_i (i = 1, 2, 3) is the fraction of interstitials occupying sublattice i. A finite size correction is performed in order to ensure the correct asymptotic behavior of the order parameter at high temperatures.

To quantitatively determine the critical temperatures at different C concentrations, we use the following asymmetric sigmoid function [49] to fit our simulation result in Fig. 3c.

$$\theta = \frac{1}{\left[1+(2^{\frac{1}{A_3}}-1)e^{A_1(T-A_2)}\right]^{A_3}} \quad (11)$$

where A_1, A_2 and A_3 are fitting parameters. After fitting, the critical temperature T_c can be determined directly by equaling $d^2\theta/d^2T$ to 0, namely,

$$T_c = \frac{1}{A_1}\ln\frac{2^{1/A_3}-1}{A_3} + A_2 \quad (12)$$

Data availability
The datasets generated during the current study are available from the corresponding authors on request.

Code availability
The computer code developed during the current study is available from the corresponding authors on request.

References
42. Plimpton, S. Fast parallel algorithms for short-range molecular dynamics. *J. Comput. Phys.* **117**, 1–19 (1995).

43. Boeck, S., Freysoldt, C., Dick, A., Ismer, L., & Neugebauer, J. The object-oriented DFT program library S/PHI/nX. *Comput. Phys. Commun.* **182**, 543–554 (2011).

44. Kresse, G. & Furthmüller, J. Efficient iterative schemes for ab initio total-energy calculations using a plane-wave basis set. *Phys. Rev. B* **54**, 11169–11186 (1996).

45. Blöchl, P. E. Projector augmented-wave method. *Phys. Rev. B* **50**, 17953–17979 (1994).

46. Perdew, J. P., Burke, K., & Ernzerhof, M. Generalized gradient approximation made simple. *Phys. Rev. Lett*. **77**, 3865–3868 (1996).

47. Monkhorst, H. J. & Pack, J. D. Special points for Brillouin-zone integrations. *Phys. Rev. B* **13**, 5188–5192 (1976).

48. Uebing, C. On the ordering of interstitials in bcc metals and bct martensites: A lattice gas approach. *Scr. Metall. Mater*. **30**, 1183–1188 (1994).

49. Finney, D. J. Bioassay and the practice of statistical inference. *Int. Stat. Rev*. **47**, 1 (1979).

Author contributions

X.Z., T.H., and J.N. designed the project. X.Z. performed all atomistic calculations under the supervision by T.H., J.R., and J.N. H.W. and Y.L. did the HRTEM characterization and APT analysis. All authors discussed the results and contributed to writing the manuscript.

Competing interests

The authors declare no competing interests.